Inorganic Chemistry

Article

pubs.acs.org/IC

Geometric and Electronic Structures of Manganese-Substituted Iron Superoxide Dismutase

Timothy A. Jackson,[†] Craig T. Gutman,[†] James Maliekal,[‡] Anne-Frances Miller,[‡] and Thomas C. Brunold*[,†]

[†]Department of Chemistry, University of Wisconsin-Madison, Madison Wisconsin 53706, United States

[‡]Department of Chemistry, University of Kentucky, Lexington, Kentucky 40506, United States

Supporting Information

ABSTRACT: The active-site structures of the oxidized and reduced forms of manganese-substituted iron superoxide dismutase (Mn(Fe)SOD) are examined, for the first time, using a combination of spectroscopic and computational methods. On the basis of electronic absorption, circular dichroism (CD), magnetic CD (MCD), and variable-temperature variable-field MCD data obtained for oxidized Mn(Fe)SOD, we propose that the active site of this species is virtually identical to that of wild-type manganese SOD (MnSOD), with both containing a metal ion that resides in a trigonal bipyramidal ligand environment. This proposal is corroborated by quantum mechanical/molecular mechanical (QM/MM) computations performed on complete protein models of Mn(Fe)SOD in both its oxidized and reduced states and, for comparison, wild-type (WT) MnSOD. The major differences between the QM/MM optimized active sites of WT MnSOD and Mn(Fe)SOD are a smaller (His)N−Mn−N(His) equatorial angle and a longer (Gln146(69))NH···O(sol) H-bond distance in the metal-substituted protein. Importantly, these modest geometric differences are consistent with our spectroscopic data obtained for the oxidized proteins and high-field electron paramagnetic resonance spectra reported previously for reduced Mn(Fe)SOD and MnSOD. As Mn(Fe)SOD exhibits a reduction midpoint potential (E_m) almost 700 mV higher than that of MnSOD, which has been shown to be sufficient for explaining the lack of SOD activity displayed by the metal-subtituted species (Vance, C. K.; Miller, A. F. *Biochemistry* **2001**, *40*, 13079−13087), E_m's were computed for our experimentally validated QM/MM optimized models of Mn(Fe)SOD and MnSOD. These computations properly reproduce the experimental trend and reveal that the drastically elevated E_m of the metal substituted protein stems from a larger separation between the second-sphere Gln residue and the coordinated solvent in Mn(Fe)SOD relative to MnSOD, which causes a weakening of the corresponding H-bond interaction in the oxidized state and alleviates steric crowding in the reduced state.

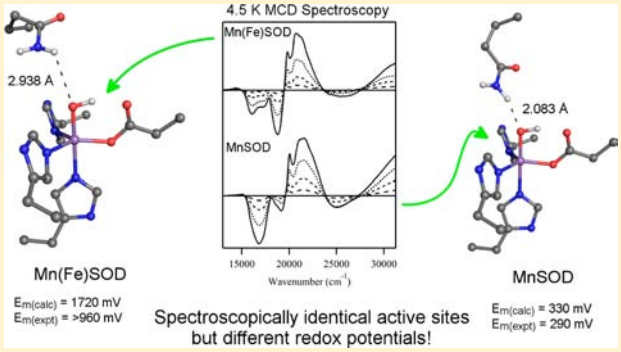

1. INTRODUCTION

Superoxide dismutases (SODs) are metalloenzymes that protect aerobic organisms from oxidative damage mediated by the superoxide radical anion ($O_2^{\bullet-}$).[1−4] To date, SODs using either Fe, Mn, Cu/Zn, or Ni metal cofactors have been identified.[3,4] While Cu/ZnSODs and NiSODs are structurally distinct, Fe- and MnSODs are homologous in terms of their overall protein folds and their active-site structures, with both containing a metal ion in a trigonal bipyramidal coordination environment consisting of two histidines (His81(73)[5] and His171(160)) and an aspartate residue (Asp167(156)) in the equatorial plane and a third histidine residue (His26) and a solvent molecule in the axial positions (Figure 1).[6,7] Spectroscopic and computational studies have afforded compelling evidence that the coordinated solvent is a hydroxide in oxidized Fe^{3+}- and Mn^{3+}SODs and a water molecule in the reduced proteins (eq 1).[8−11] In addition to the structural similarities between Fe- and MnSODs, both of these enzymes (and, in fact, all known SODs) employ a two-step ping-pong mechanism for catalyzing the disproportionation of $O_2^{\bullet-}$ at rates approaching the diffusion-controlled limit (eq 2, wherein M is the Fe or Mn ion of Fe and MnSODs and the superscript indicates the nature of the solvent molecule coordinated to the metal ion).[12−15]

$$M^{3+}SOD^{OH} + e^- + H^+ \rightarrow M^{2+}SOD^{H2O} \quad (1)$$

$$M^{3+}SOD^{OH} + O_2^{\bullet-} + H^+ \rightarrow M^{2+}SOD^{H2O} + O_2 \quad (2a)$$

$$M^{2+}SOD^{H2O} + O_2^{\bullet-} + H^+ \rightarrow M^{3+}SOD^{OH} + H_2O_2 \quad (2b)$$

While some SODs are catalytically active with either iron or manganese bound to their active sites (the so-called cambialistic SODs), an overwhelming majority of these enzymes are metal ion specific, meaning that iron substituted into a MnSOD

Received: December 31, 2012
Published: March 5, 2013

   dx.doi.org/10.1021/ic302867y | *Inorg. Chem.* 2013, 52, 3356−3367

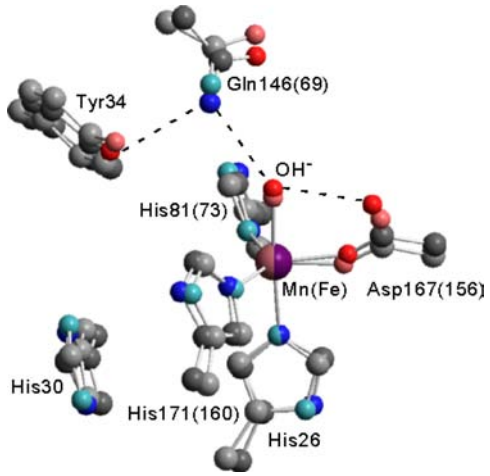

Figure 1. Overlay plot of the active sites of Mn^{3+}SOD (dark) and Fe^{3+}SOD (light), based on PDB files 1VEW and 1ISB, respectively.[6,7] The numbering schemes relate to *E. coli* MnSOD and, in parentheses, FeSOD if different. Active-site H-bonding interactions are indicated by dashed lines.

protein matrix (referred to as Fe(Mn)SOD) and vice versa (Mn(Fe)SOD) yields inactive proteins.[2,16,17] A number of intriguing differences between WT and metal-substituted SODs have been identified (e.g., altered active-site p*K* values and affinities for OH^- binding)[18,19] and have led to several proposed reasons for the observed metal-ion specificity, including an increased anion affinity of Fe(Mn)SOD, active site distortions upon binding of the non-native metal ion (Figure 2), and inappropriate reduction midpoint potentials (E_m's) of the metal substituted enzymes.

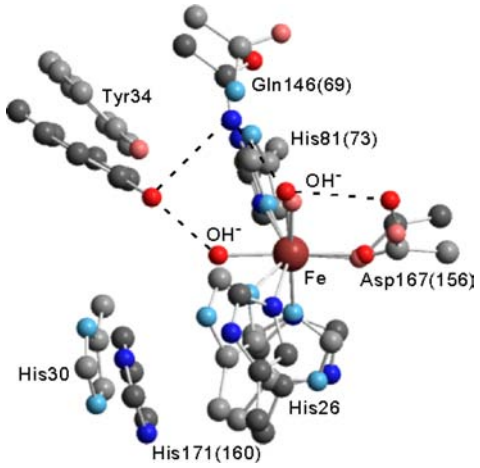

Figure 2. Overlay plots of active sites of Fe^{3+}(Mn)SOD (dark) and Fe^{3+}SOD (light), based on PDB files 1MMM (subunit B) and 1ISB, respectively.[6,91] The numbering schemes relate to *E. coli* MnSOD and, in parentheses, FeSOD if different. Active-site H-bonding interactions for Fe^{3+}(Mn)SOD are indicated by dashed lines.

To perform both the reduction and the oxidation of $O_2^{\bullet-}$, Fe- and MnSODs must possess E_m values between those associated with the reduction of $O_2^{\bullet-}$ to H_2O_2 ($E_m \approx 890$ mV at pH 7)[20] and the oxidation of $O_2^{\bullet-}$ to O_2 ($E_m \approx -160$ mV at pH 7).[2] Because the E_m of Fe(Mn)SOD ($E_m \approx -250$ mV at pH 7.8)[21] and Mn(Fe)SOD ($E_m > 960$ mV at pH 7.8)[22] from *E. coli* are too low and too high, respectively, for catalytic turnover, Vance et al. suggested that the lack of SOD activity of the metal-substituted enzymes stems from their E_m's lying outside the range required for catalyzing both half-reactions (eq 2).[21,22] This proposal was corroborated by our spectroscopic characterization of FeSOD and Fe(Mn)SOD, which revealed that incorporation of Fe into the (Mn)SOD protein matrix preserves the native five-coordinate active-site environment.[23] More recently, we have performed combined quantum mechanical/molecular mechanical (QM/MM) geometry optimizations on entire protein models of Fe-bound SOD species and employed density functional theory (DFT) to compute redox potentials for the corresponding active sites. These computations provided clear evidence that the positioning of a second-sphere Gln residue (Gln69 and Gln146 for Fe- and MnSODs, respectively), which H-bonds with coordinated solvent (Figure 1), is the major contributor to the different redox tunings of Fe- and MnSODs.[24]

While Fe(Mn)SOD has been the subject of several studies,[18,19,21,25] Mn(Fe)SOD has been characterized only sparingly. On the basis of the close resemblance of the absorption spectra of Mn^{3+}SOD and Mn^{3+}(Fe)SOD, it was suggested that the respective active sites possess similar structures.[22] However, recent high-field and high-frequency electron paramagnetic resonance (HF EPR) studies revealed different zero-field splitting (ZFS) parameters for Mn^{2+}SOD and Mn^{2+}(Fe)SOD.[26] These differences in ZFS parameters were attributed to differences in second-sphere and/or electrostatic interactions, although it was noted that they could also be caused by alterations in the first coordination sphere.[26] These ambiguities primarily stem from the fact that the active-site structures of both reduced and oxidized Mn(Fe)SODs remain poorly defined, as Mn(Fe)SOD has thus far eluded characterization by X-ray crystallography. Consequently, the structural basis for the dramatically elevated E_m of Mn(Fe)SOD[22] remains largely unexplored.

In this study, we have employed electronic absorption, circular dichroism (CD), magnetic CD (MCD), and variable-temperature, variable-field (VTVH) MCD spectroscopies to probe the electronic transitions and estimate ZFS parameters for *E. coli* Mn^{3+}(Fe)SOD. These experimental data were used along with published ZFS parameters of Mn^{2+}(Fe)SOD to evaluate active-site models of Mn(Fe)SOD in both its oxidized and reduced states that were generated from the published X-ray crystal structures of *E. coli* FeSOD[6] by using QM/MM whole protein geometry optimizations. These experimentally validated models were then used to compute the E_m of Mn(Fe)SOD relative to that of MnSOD, using an approach whereby the electrostatic interactions between the active site and more remote amino acid residues were explicitly accounted for. Collectively, our spectroscopic and computational results provide significant new insight into the mechanism of active-site redox tuning employed by Fe- and MnSODs.

2. MATERIALS AND METHODS

2.1. Sample Preparation. FeSOD was purified from *E. coli* according to standard procedures.[21,27,28] Mn(Fe)SOD was generated starting from FeSOD according to a slightly modified version[22] of a protocol developed by Yamakura.[17] Mn(Fe)SOD was isolated in the reduced, Mn^{2+}-bound state and was oxidized by incubation with a slight molar excess of potassium permanganate ($KMnO_4$). In parallel experiments, we found that treatment of as-isolated Mn^{3+}SOD with $KMnO_4$ did not notably affect the spectroscopic properties of this species, indicating that $KMnO_4$ oxidation of the metal ion does not cause any major damage to the SOD active site.

dx.doi.org/10.1021/ic302867y | *Inorg. Chem.* 2013, 52, 3356−3367

2.2. Absorption, CD, and MCD Spectroscopies. Room temperature absorption spectra were collected on a Cary 5E spectrometer. Variable temperature CD and low temperature absorption and MCD spectra were obtained using a spectropolarimeter (Jasco J-715) in conjunction with a magnetocryostat (Oxford Instruments SM-4000). Samples of Mn^{3+}(Fe)SOD for room-temperature measurements were ~0.77 mM in protein and contained 50 mM phosphate buffer (pH 7.0). Samples used for low-temperature studies were mixed with glycerol (~55% v/v) to ensure glass formation upon freezing. Variable temperature, variable field (VTVH) MCD data obtained for Mn^{3+}SOD and Mn^{3+}(Fe)SOD were analyzed using a fitting program developed by Dr. Frank Neese (MPI Mülheim, Germany)[29] to determine zero-field splitting (ZFS) parameters for the Mn^{3+} center and the polarization of the transition under study. To explore the complete parameter space, the axial ZFS parameter D was systematically varied from −3 to 3 cm^{-1} in steps of 0.5 cm^{-1}, and for each D value the rhombicity (E/D) was varied from 0 to 0.33 in increments of 0.11. For each set of D and E/D values, the transition moment products (M_{xy}, M_{xz}, and M_{yz}, where the coordinate system is defined by the principal axes of the **D**-tensor) were optimized to fit the experimental data, and the goodness of fit was assessed by the χ^2 value, which is the sum of the squares of the differences between the predicted and experimental data. All g-values were assumed to be 2.00, as deviations from this free electron value are typically minor (i.e., ~0.05) for Mn^{3+} complexes and, thus, too small to noticeably affect the VTVH MCD saturation behavior (also note that variations in g-values within reasonable limits were found not to significantly affect the χ^2 values of our fits). This fitting procedure has been shown previously to permit accurate determination of both ZFS parameters and transition polarizations for metalloenzymes and transition metal complexes.[30−32]

2.3. Computations. *(A). Generation of Model Systems.* The protein models for oxidized and reduced *E. coli* MnSOD ($Mn^{3+}SOD_{1VEW}$ and $Mn^{2+}SOD_{1VEW}$, respectively) were derived from the X-ray structure coordinates of monomer A of the redox heterogeneous MnSOD tetramer from *E. coli* (PDB file 1VEW).[7] Models of oxidized and reduced Mn(Fe)SOD (Mn^{3+}(Fe)SOD_{1ISB} and Mn^{2+}(Fe)SOD_{1ISA}, respectively) were based on monomer A of the X-ray structures of *E. coli* Fe^{3+}SOD (PDB file 1ISB) and Fe^{2+}SOD (PDB file 1ISA),[6] respectively, where in each case manganese was substituted for iron in the active site (Figure 2).

The pdb2adf program developed by Swart and provided by Scientific and Computer Modeling (SCM) was used to add protons to all protein models and to convert the corresponding PDB files into a format compatible with the Amsterdam Density Functional (ADF) 2003.01 software package.[33−35] On the basis of the results obtained in previous studies of MnSODs,[8−11,30] the axial solvent ligand (Figure 1) was modeled as OH^- in the Mn^{3+}-bound SODs and as H_2O in the Mn^{2+}-bound SODs.

(B). QM/MM Geometry Optimizations. All MnSOD and Mn(Fe)-SOD models described in the previous section were energy minimized with respect to all atomic positions using the QM/MM method as implemented in the ADF software package.[33−35] The entire first coordination sphere and the second-sphere residues Gln146(69) and Tyr34 were treated at the QM level, with the QM/MM interface bisecting the C_α−NH and C_α−CO bonds; that is, the C_α atoms and their H atoms were included in the QM region, whereas the NH and CO groups of the amide backbone were assigned to the MM region. The QM region was treated using a basis set consisting of uncontracted triple-ζ Slater-type orbitals including a single set of polarization functions (ADF basis set IV), an integration constant of 3.0, and the local density approximation of Vosko, Wilk, and Nusair[36] with the nonlocal gradient corrections of Becke[37] and Perdew.[38] Core orbitals were frozen through 1s (O, N, C) and 2p (Mn). All other residues and the crystallographically detected water molecules associated with the protein monomer were treated using the AMBER95 force field,[39] which was augmented with suitable parameters for manganese.[40] The integrated molecular orbital and molecular mechanics (IMOMM) approach of Maseras and Morokuma[41,42] was used to describe the QM/MM interface. Electrostatic coupling between the QM and MM regions was accounted for by employing pure MM coupling, whereby the MM region was not allowed to polarize the QM wave function, though the point charges of the QM region were updated throughout the energy minimization using the multipole derived charge analysis developed by Swart et al.[43] As the energy of the MM region usually converged within ~1000 optimization cycles (i.e., the energy difference between 1000 and 10 000 MM cycles was <1 kcal/mol), 1000 MM optimizations were typically performed per QM cycle. It should be noted that in some cases, however, as many as 5000 MM optimizations were required per QM cycle to ensure reasonable convergence of the MM region. The protein models were considered converged when the maximum energy gradients on the QM atoms dropped below 0.007 au/Å and the change in QM energy between two consecutive cycles fell below 0.001 au. Cartesian coordinates for the QM regions of all optimized protein models are provided in the Supporting Information, Tables S1−S4.

(C). Calculation of Ground-State and Excited-State Properties. The ORCA 2.2 software package, developed by Dr. Frank Neese,[44] was used to perform semiempirical INDO/S−CI and time-dependent (TD) DFT computations on the active sites of our QM/MM optimized protein species. All active-site models used for INDO/S−CI computations included the first coordination sphere as well as Gln146(69) and Tyr34. Each residue was truncated by replacing its C_α atom with a hydrogen and reducing the corresponding C_β−H bond length to 1.113 Å. For TD-DFT computations, only the first coordination sphere was included, as previous studies have shown that the removal of Tyr34 and Gln146(69) has negligible effects on TD-DFT computed absorption spectra of Mn^{3+}SODs.[45]

The INDO/S−CI method as implemented in the ORCA program employs the model of Zerner and co-workers,[46,47] the valence shell ionization potentials and Slater−Condon parameters listed by Bacon and Zerner,[48] the standard interaction factors $f_{p\sigma p\sigma}$ = 1.266 and $f_{p\pi p\pi}$ = 0.585, and the following spin−orbit coupling constants: ζ_{3d}(Mn) = 300 cm^{-1}, ζ_{4p}(Mn) = 334 cm^{-1}, ζ_{2p}(N) = 76 cm^{-1}, ζ_{2p}(O) = 150 cm^{-1}. Restricted open-shell Hartree−Fock self-consistent field calculations for the Mn^{3+}- and Mn^{2+}-containing active-site models were tightly converged on the quintet and sextet ground states, respectively. For our Mn^{3+}-containing models, configuration interaction (CI) with single and double electron excitations (CISD) was then included within the S = 2 spin-state manifold and CI with single electron excitations (CIS) was included within the S = 1 spin-state manifold. Alternatively, for our Mn^{2+}-containing models, CISD and CIS were included within the S = 5/2 and S = 3/2 spin-state manifolds, respectively. The CI active spaces used for all INDO/S−CI computations performed in this study are provided in the Supporting Information. In all cases, the completeness of these active spaces was monitored by the insensitivity of the calculated zero-field splitting parameters to the inclusion of additional one- and two-electron excitations.

TD-DFT calculations[49−51] using the ORCA program were performed as spin unrestricted and employed Becke's three-parameter hybrid functional for exchange[52,53] combined with the Lee−Yang−Parr correlation functional[54] (referred to as B3LYP/G in ORCA) and the default 20% Hartree−Fock exchange. The SV(P) (Ahlrichs polarized split valence) basis set[55,56] with the SV/C auxiliary basis set[57] were used for all atoms except Mn, for which the TZVP (Ahlrichs polarized triple-ζ valence) basis set[56,58] in conjunction with the TZV/J auxiliary basis set were used. The size of the integration grid chosen for all calculations was 3 (Lebedev 194 points). For all TD-DFT calculations the Tamm-Dancoff approximation[59,60] was used along with the resolution of the identity approximation in calculating the Coulomb term[61] to facilitate convergence. In each case, 40 excited states were calculated by including all one-electron excitations within an energy window of ±3 hartree with respect to the HOMO/LUMO energies.

(D). Natural Bond Orbital Calculations. Natural bond orbital (NBO) calculations[62,63] were performed using the NBO 5.0 program[64] as implemented in the Gaussian 98 software package.[65] Single-point DFT calculations were performed using the spin-unrestricted B3LYP hybrid functional (UB3LYP)[52−54] and the Pople-style 6-31G* (for C,

dx.doi.org/10.1021/ic302867y | Inorg. Chem. 2013, 52, 3356−3367

N, and H)[66−70] and 6-311G* (for Mn and O)[71−73] basis sets. To facilitate convergence, initial single-point computations were performed with the UB3LYP functional using the smaller 3-21G basis set[74−79] for all atoms, and the resulting checkpoint files were utilized as initial guesses for subsequent computations using the larger basis sets. All computations were tightly converged on the quintet or sextet ground states of the Mn^{3+}- and Mn^{2+}-containing models, respectively.

Within the NBO formalism, a H-bond is viewed as a charge transfer from the occupied H-bond donor NBO (σ_d) to the unoccupied H-bond acceptor NBO (σ_a*).[62,63] The strength of this H-bonding interaction is quantitatively described using second-order perturbation theory according to eq 3,

$$\Delta E^{(2)}_{d\rightarrow a} = -2\frac{\langle \sigma_d|\hat{\mathbf{F}}|\sigma_a^*\rangle^2}{\varepsilon_a - \varepsilon_d} \quad (3)$$

where $\hat{\mathbf{F}}$ is the Kohn−Sham operator, ε_d and ε_a are the orbital energies of the σ_d and σ_a* NBOs, respectively, and $\Delta E^{(2)}_{d\rightarrow a}$ is the energetic stabilization of the σ_d NBO due to the admixture of σ_a* orbital character.[62,63] As the matrix element in eq 3 is proportional to the overlap integral of the corresponding pre-NBOs, $\langle \sigma_{pre-d}|\sigma^*_{pre-a}\rangle$,[80] plots of the pre-NBOs of interest provide qualitative insight into the strength of the H-bonding interaction; that is, pre-NBOs with significant overlap correspond to large $\Delta E^{(2)}_{d\rightarrow a}$values and thus reflect strong H-bonds. Pre-NBOs were plotted using the NBOView program developed by Wendt and Weinhold.[81] All NBO analyses were carried out using the choose option that permits the user to define NBO resonance structures, which was necessary to afford the proper resonance description of histidine ligands.

(E). Calculation of Reduction Potentials. Reduction midpoint potentials for MnSOD and Mn(Fe)SOD were computed following an approach developed by Noodleman and co-workers[11,82−85] with some modifications, as described briefly below. For redox processes involving proton and electron transfers (eq 1), it is convenient to separate the energetic contributions from these steps by considering the energies of $Mn^{3+}SOD^{OH} \rightarrow Mn^{2+}SOD^{OH}$ reduction (eq 4) and $Mn^{2+}SOD^{OH} \rightarrow Mn^{2+}SOD^{H2O}$ protonation (eq 5). The electron transfer energy (ε_{ET}, eq 4a), which is the energy required for the first process, contains contributions from the gas-phase ionization potential ($IP_{(g)}$, in eV) of $Mn^{2+}SOD^{OH}$ (eq 4b) and the changes in protein and reaction field energies that accompany metal ion reduction ($\Delta\varepsilon_{pr\text{-}ET}$, eq 4c). The latter contribution incorporates the electrostatic interactions of the active site with the remainder of the protein and bulk solvent. ε_{ET} is conventionally expressed relative to the potential of the normal hydrogen electrode (−4.43 V in eq 4a).

$$\varepsilon_{ET} = IP_{(g)} + \Delta\varepsilon_{pr\text{-}ET} - 4.43V \quad (4a)$$

$$IP_{(g)} = E[Mn^{3+}SOD^{OH}] - E[Mn^{2+}SOD^{OH}] \quad (4b)$$

$$\Delta\varepsilon_{pr\text{-}ET} = E_{pr\text{-}ET}[Mn^{3+}SOD^{OH}] - E_{pr\text{-}ET}[Mn^{2+}SOD^{OH}] \quad (4c)$$

The proton transfer energy associated with the $Mn^{2+}SOD^{OH} \rightarrow Mn^{2+}SOD^{H2O}$ conversion (ε_{PT}) is determined by the p*K* value of the coordinated water ligand of $Mn^{2+}SOD^{H2O}$ (eq 5a). Note that this p*K* value must be corrected for the pH of the medium (here we have assumed a pH of 7.8 to permit a direct comparison with experimental data) and that the factors of 1.37 and 23.06 are used to convert from pH units to kcal/mol and then to eV, respectively (eq 5a). The calculation of the p*K* value for $Mn^{2+}SOD^{H2O}$ (eq 5b) requires evaluation of three contributions: (i) the gas-phase proton affinity ($PA_{(g)}$, eq 5c), which itself contains contributions from the deprotonation energy of $Mn^{2+}SOD^{H2O}$, the difference in zero-point energies (ΔZPE) of the deprotonated and protonated states (ΔZPE ≈ −7.1 kcal/mol for Mn^{2+} complexes[82]), and a work term; (ii) the difference in protein and reaction field energies of the $Mn^{2+}SOD^{OH}$ and $Mn^{2+}SOD^{H2O}$ states ($\Delta\varepsilon_{pr\text{-}PT}$, eq 5d); and (iii) a correction term of −267.7 kcal/mol associated with the free energy of a proton in aqueous solution. The reduction midpoint potential incorporating both electron and proton transfer steps is the sum of the electron and proton transfer energies (eq 6).

$$\varepsilon_{PT} = \frac{1.37\{pK[Mn^{2+}SOD^{H2O}] - 7.8\}}{23.06} \quad (5a)$$

$$1.37pK[Mn^{2+}SOD^{H2O}] = PA_{(g)} + \Delta\varepsilon_{pr\text{-}PT} - 267.7 \quad (5b)$$

$$PA_{(g)} = E[Mn^{2+}SOD^{OH}] + E[H^+] - E[Mn^{2+}SOD^{H2O}] + \Delta ZPE + \frac{5}{2}RT \quad (5c)$$

$$\Delta\varepsilon_{pr\text{-}PT} = E_{pr\text{-}EP}[Mn^{2+}SOD^{OH}] - E_{pr\text{-}PT}[Mn^{2+}SOD^{H2O}] \quad (5d)$$

$$E_m = \varepsilon_{ET} + \varepsilon_{PT} \quad (6)$$

Because current versions of ADF do not implement correct electrodynamic coupling (i.e., the MM point charges do not polarize the QM wave functions),[86] the energies for calculating E_m were obtained by performing DFT single-point calculations on the full QM region of our QM/MM geometry optimized protein models using ORCA 2.9.[87] These calculations employed the same functionals and basis sets as the TD-DFT computations described above with the exception that the TZVP basis set was used for the Mn ion as well as all ligating nitrogen and oxygen atoms. To account for differences in protein field energies, which depend on active-site/protein electrostatic interactions, the point charge correction routine in ORCA was employed using the point charges from the MM region of our QM/MM optimized protein models. Differences in reaction field energies of the MnSOD active sites, which depend on active-site/solvent interactions, are expected to be independent of the active-site oxidation and protonation states because of the buried nature of the active site,[6,7] and thus we have considered these differences to be negligible. Therefore, in computing E_m we have assumed that the $\Delta\varepsilon_{pr\text{-}ET}$ and $\Delta\varepsilon_{pr\text{-}PT}$ terms are sufficiently accounted for in our DFT single-point calculations with point charge corrections. As the $E[Mn^{2+}SOD^{OH}]$ terms cancel upon summation of the ε_{ET} and ε_{PT} contributions (eq 6), the only terms required for determining E_m are $E[Mn^{3+}SOD^{OH}]$, $E[Mn^{2+}SOD^{H2O}]$, and $E[H^+]$ = 291.762 kcal/mol, where the latter value was chosen on the basis of previous DFT studies.[11] $E[Mn^{3+}SOD^{OH}]$ and $E[Mn^{2+}SOD^{H2O}]$ were obtained from the DFT single-point calculations with point charge corrections described above.

3. RESULTS AND ANALYSIS

3.1. Spectroscopic Properties of Mn(Fe)SOD and MnSOD. *(A). Oxidized States.* The absorption and CD spectra of *E. coli* Mn^{3+}(Fe)SOD obtained at 300 and 4.5 K (Figure 3, top and center) are quite similar, the only differences being the increased intensities and slightly higher energies of the features in the 4.5 K spectra. These differences are due to the decreased nuclear motion at 4.5 K, which leads to a sharpening and, typically, a small blue-shift of each band,[88] and do not reflect any major changes in coordination geometry as temperature is lowered. Most importantly, the absorption, CD, and MCD spectra of Mn^{3+}(Fe)SOD are strikingly similar to those of WT Mn^{3+}SOD that are shown for comparison in Figure 4. In light of these spectral similarities (cf. Figures 3 and 4), the results obtained in previous spectroscopic and computational studies of WT Mn^{3+}SOD will be briefly reviewed to establish a suitable basis for a quantitative comparison of the spectroscopic properties of Mn^{3+}SOD and Mn^{3+}(Fe)SOD.

Detailed analyses of the low-temperature absorption, CD, and MCD spectra of *E. coli* Mn^{3+}SOD (Figure 4) have revealed that the energies of the spin-allowed d → d transitions of the active-site Mn^{3+} ion (Table 1), which span the 15 000−25 000 cm^{-1} spectral range, reflect a trigonal bipyramidal ligand environment,[45,89,90] consistent with the X-ray crystal structure of this enzyme (Figure 1).[7] All spectroscopic features between

dx.doi.org/10.1021/ic302867y | Inorg. Chem. 2013, 52, 3356−3367

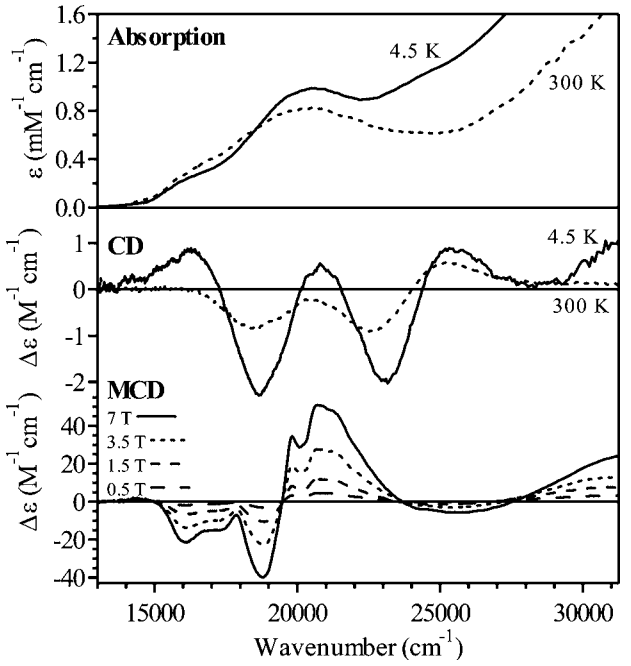

Figure 3. Absorption (top) spectra at 300 and 4.5 K and CD (center) spectra and 4.5 K, variable-field MCD spectra (bottom) of Mn^{3+}(Fe)SOD. Conditions: 0.77 mM Mn^{3+}(Fe)SOD in 50 mM phosphate buffer (pH 7.0) and 55% (v/v) glycerol.

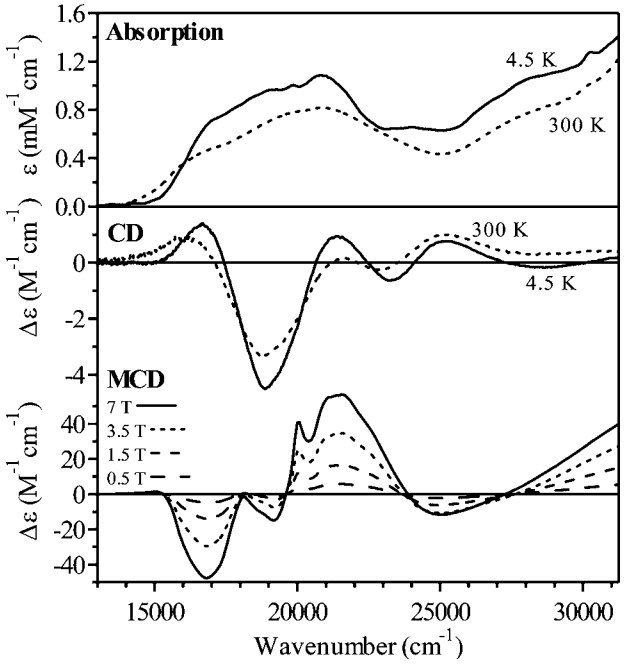

Figure 4. Absorption (top) spectra at 300 and 4.5 K and CD (center) spectra and 4.5 K, variable-field MCD spectra (bottom) of Mn^{3+}SOD. Conditions: 2 mM Mn^{3+}SOD in 50 mM phosphate buffer (pH 7.0) and 55% (v/v) glycerol.

25 000 and 32 000 cm^{-1} (Figure 4) are due to ligand-to-metal charge transfer (LMCT) transitions.[45,90] Specifically, on the basis of time-dependent (TD) DFT computations[45] and polarized single-crystal absorption studies of Mn^{3+}SOD,[90] the dominant features in the near-UV spectral region were attributed to $Asp^{-} \rightarrow Mn^{3+}$ charge-transfer (CT) transitions.

Table 1. Experimental Mn^{3+} d → d Transition Energies[a] for Oxidized WT Mn^{3+}SOD and Mn^{3+}(Fe)SOD and Zero-Field Splitting Parameters[b] for Reduced Mn^{2+}SOD and Mn^{2+}(Fe)SOD

	WT Mn^{3+}SOD	Mn^{3+}(Fe)SOD
d → d	16 900	16 470
d → d	19 025	18 770
d → d	21 100	20 670
d → d	23 300	23 100
	WT Mn^{2+}SOD	Mn^{2+}(Fe)SOD
$\lvert D\rvert$	0.3548	0.3506
E/D	0.0860	0.0405

[a]Experimental transition energies based on Gaussian deconvolutions of low-temperature absorption, CD, and MCD data.[45] [b]Experimental ZFS parameters based on HF-EPR studies (ref 26).

The Mn^{3+} d → d transition energies obtained from a Gaussian analysis of our low-temperature absorption, CD, and MCD spectra of Mn^{3+}(Fe)SOD are remarkably similar to those determined previously for Mn^{3+}SOD[45] (Table 1). For comparison, MCD spectra reported for $[MnCl_5]^{2-}$, a square pyramidal Mn^{3+} system, exhibit prominent pseudo-*A* terms at ~16 000 and 25 000 cm^{-1},[89] spectral signatures distinctly different from those observed for Mn^{3+}(Fe)SOD (Figure 3, bottom). Collectively, these results indicate that the active-site structure of Mn^{3+}(Fe)SOD is virtually identical to that of Mn^{3+}SOD, in support of a previous proposal based on a qualitative comparison of the absorption spectra of these proteins.[22] Thus, while X-ray structural data of Fe^{3+}(Mn)-SOD[91] reveal an altered metal coordination geometry relative to WT Fe^{3+}SOD,[6] our excited-state spectroscopic data obtained for Mn^{3+}(Fe)SOD argue against major active-site distortions for this metal-substituted SOD.

In addition to the similar electronic absorption, CD, and MCD spectra of Mn^{3+}SOD and Mn^{3+}(Fe)SOD (cf. Figures 3 and 4), variable-temperature variable-field MCD data obtained at 20 202 and 20 690 cm^{-1}, respectively, are virtually superimposable (Figure 5, top and center). Considering that VTVH MCD data for $S > 1/2$ systems are a sensitive function of transition polarization and ground-state zero-field splitting (ZFS) parameters,[29,92] the high resemblance of these two data sets (Figure 5) demonstrates that the Mn^{3+}SOD and Mn^{3+}(Fe)SOD active sites also possess comparable ground-state properties. The VTVH MCD data were quantitatively analyzed to determine the set of axial (D) and rhombic (E) ZFS parameters and transition polarizations that best fit the experimental data, as assessed by the χ^2 value that is defined as the sum of the squares of the differences between simulated and experimental data. In the case of Mn^{3+}SOD, the best fits ($\chi^2 <$ 0.03) were obtained with $D = +2.0-2.5$ cm^{-1} and $E/D = 0-0.33$, or $D = -2.5$ to -3 cm^{-1} and $E/D > 0.11$ (Supporting Information, Figure S1). Similar results were obtained for Mn^{3+}(Fe)SOD, where χ^2 dropped below 0.02 for $D = +2.0$ cm^{-1} and $E/D \geq 0.11$, or $D = -2.5$ to -3 cm^{-1} and $E/D \geq 0.11$ (Supporting Information, Figure S2). For each species the predicted transition moments were found to depend on the sign of D; that is, for $D < 0$ cm^{-1} predominantly (>80%) z-polarization was predicted, whereas fits with $D > 0$ cm^{-1} yielded a transition moment with a rather large (>70%) y-component (Supporting Information, Tables S5 and S6).[93] Parallel mode EPR studies of Mn^{3+}SOD have revealed that $D = +2.10$ cm^{-1} and $E/D = 0.114$ for this species,[94] where, according to ligand-

dx.doi.org/10.1021/ic302867y | Inorg. Chem. 2013, 52, 3356−3367

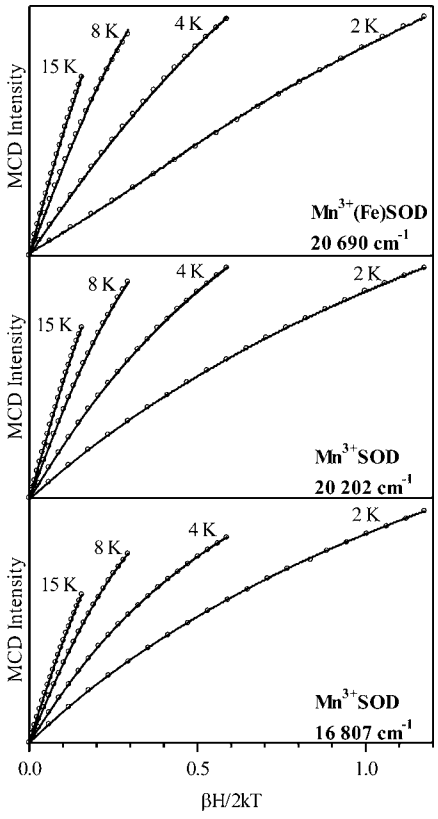

Figure 5. Top: Experimental VTVH MCD data collected at 20 690 cm^{-1} (483 nm) for Mn^{3+}(Fe)SOD (solid lines) and theoretical fit (○) using the following parameters: D = 2 cm^{-1}, E/D = 0.20, $g_{x,y,z}$ = 2.00, and 2% x-, 98% y-, and <1% z-polarization. Center: Experimental VTVH MCD data collected at 20 202 cm^{-1} (495 nm) for Mn^{3+}SOD (solid lines) and theoretical fit (○) using the following parameters: D = 2 cm^{-1}, E/D = 0.10, $g_{x,y,z}$ = 2.00, and 29% x-, 70% y-, and 1% z-polarization. Bottom: Experimental VTVH MCD data collected at 16 807 cm^{-1} (595 nm) for Mn^{3+}SOD (solid lines) and theoretical fit (○) using the following parameters: D = 2 cm^{-1}, E/D = 0.10, $g_{x,y,z}$ = 2.00, and 21% x-, 73% y-, and 7% z-polarization. See captions of Figures 3 and 4 for sample conditions.

field theory, the positive sign of D is in agreement with the trigonal bipyramidal active-site geometry.[7] Because the Mn^{3+} d → d transition energies of Mn^{3+}(Fe)SOD also reflect a trigonal bipyramidal ligand environment, it can be concluded that D is positive for this species as well. On the basis of these considerations, we conclude that the VTVH MCD data obtained for both Mn^{3+}(Fe)SOD and Mn^{3+}SOD are consistent with $D \geq +2$ cm^{-1}, $E/D > 0.1$, and a predominantly y-polarized transition moment. It is important to note, however, that our analysis does not provide a precise value for E/D (Supporting Information, Figures S1 and S2). For example, fits of the VTVH MCD data obtained for Mn^{3+}(Fe)SOD with D = 2 cm^{-1} and E/D = 0.15 or 0.25 yield similar χ^2 values ($\chi^2 \approx$ 0.008), the only difference being a slightly larger (~8%) y-component predicted for the transition moment of the more rhombic system.

Interestingly, the VTVH MCD data sets of Mn^{3+}SOD collected at 20 202 cm^{-1} and, previously,[30] at 16 807 cm^{-1} (Figure 5, center and bottom) show small but noticeable differences in terms of the MCD signal saturation behavior at low temperature. Specifically, while the 4 and 8 K isotherms collected at 20 202 cm^{-1} display similar high-field MCD signal intensities as the 2 K isotherm (Figure 5, center), this is not the case for the data collected at 16 807 cm^{-1} (Figure 5, bottom). By comparing fits with ZFS parameters similar to those obtained from parallel mode EPR studies of Mn^{3+}SOD,[94] it is evident that the difference in saturation behavior is successfully accounted for by a small change (~6%) from z- to x-polarization (Figure 5, center and bottom), revealing the that Mn^{3+} d → d transitions centered at 16 900 and 21 100 cm^{-1} are similarly polarized. This result concurs nicely with single-crystal polarized absorption data of Mn^{3+}SOD, which also showed both of these transitions to have similar polarization ratios with respect to the Mn−O(Asp167) bond vector.[90]

(B). Reduced States. As the active-site Mn^{2+} ions of Mn^{2+}SOD and Mn^{2+}(Fe)SOD have a high-spin $3d^5$ electronic configuration, all d → d transitions are spin-forbidden and thus possess negligible absorption, CD, and MCD intensities.[89] In contrast, HF-EPR spectra of Mn^{2+}SODs and synthetic Mn^{2+} complexes are in general quite rich in information, providing considerable insight into the ground-state electronic structure of the Mn^{2+} ion.[26,95−97] Un et al. used HF-EPR spectroscopy to study Mn^{2+}SOD and Mn^{2+}(Fe)SOD from *E. coli* and determined ground-state ZFS parameters for each system (Table 1, bottom).[26] Both enzymes exhibit similar $|D|$ values of ~0.35 cm^{-1}, which correlate well with the empirical trend that five-coordinate Mn^{2+} complexes tend to possess D values greater than 0.2 cm^{-1} in magnitude.[95] The rhombicities of Mn^{2+}SOD and Mn^{2+}(Fe)SOD are, however, significantly different, with the former being about twice as large as the latter (Table 1).[26] While the exact structural basis for this difference in rhombicity is currently unclear, the ZFS parameters reported for Mn^{2+}SOD and Mn^{2+}(Fe)SOD are well suited for evaluating active-site models generated using the combined QM/MM approach described next.

3.2. QM/MM Computations for MnSOD and Mn(Fe)-SOD. While previous studies have shown that small active-site models of Mn^{3+}SOD derived from X-ray crystallographic data are effective in reproducing key spectroscopic features of this enzyme,[45,90,98] a different strategy must be used to construct active-site models of Mn^{3+}(Fe)SOD and Mn^{2+}(Fe)SOD, as no X-ray crystal structures of these species are currently available. Therefore, we have used QM/MM computations to predict complete protein structures of the oxidized and reduced states of Mn(Fe)SOD as well as of WT MnSOD, which provided a well-characterized reference system for assessing the feasibility of this approach.

(A). Geometric Structures of Mn^{3+}SOD and Mn^{3+}(Fe)SOD Models. Before comparing the active-site structures of our QM/MM optimized models of *E. coli* Mn^{3+}SOD and Mn^{3+}(Fe)SOD (referred to as $Mn^{3+}SOD_{1VEW}$ and Mn^{3+}(Fe)-SOD_{1ISB}, respectively), the efficacy of the QM/MM method for predicting reasonable protein structures was tested on the basis of our $Mn^{3+}SOD_{1VEW}$ model, as an X-ray crystal structure of this enzyme is available.[7] This test was carried out using the program PROCHECK[99,100] that allows for a comparison of protein structures on a quantitative level. PROCHECK expresses the overall normality of protein structures in terms of the so-called G factor, which is assessed on the basis of a variety of geometric parameters such as dihedral angles, peptide bond planarity, and main-chain bond angles and lengths. G factors below −1 mark protein structures of poor quality, whereas G factors greater than −0.5 are indicative of acceptable structures.[99,100] The G factors determined for subunit A of the *E. coli* Mn^{3+}SOD X-ray crystal structure and our $Mn^{3+}SOD_{1VEW}$ model are 0.23 and −0.20, respectively, indicating that our

dx.doi.org/10.1021/ic302867y | Inorg. Chem. 2013, 52, 3356−3367

Table 2. Relevant Structural and Zero-Field Splitting Parameters for Mn^{3+}SOD and Mn^{3+}(Fe)SOD

	E. coli Mn^{3+}SOD experimental[a]	$Mn^{3+}SOD_{1VEW}$ QM/MM	$Mn^{3+}(Fe)SOD_{1ISB}$ QM/MM
Mn−O(sol)	2.24	1.79	1.78
Mn−O(Asp167(156))	2.05	1.94	1.91
Mn−N(His26)	2.19	2.07	2.07
Mn−N(His171(160))	2.19	2.15	2.15
Mn−N(His81(73))	2.25	2.13	2.10
(His81(73))N−Mn−N(His171(160))	129°	126°	110°
(His81(73))N−Mn−N(Asp167(156))	110°	108°	117°
(His171(160))−Mn−N(Asp167(156))	120°	125°	132°
O(sol)−Mn−N(His26)	175°	179°	178°
O(sol)···O(Asp167(156))	2.75	2.69 (1.71)[b]	2.73 (1.77)[b]
(Gln146(69))N···O(sol)	2.89	3.07 (2.08)[b]	3.62 (2.94)[b]
(Gln146(69))N···O(Tyr34)	3.00	3.04 (2.26)[b]	3.01 (2.02)[b]
zero-field splitting parameters			
D (cm^{-1})	2.10[c]	1.18[d]	1.23[d]
E/D	0.114[c]	0.099[d]	0.203[d]

[a]Derived from the X-ray crystal structure of *E. coli* MnSOD (PDB file 1VEW).[7] [b]The corresponding H···O hydrogen-bond distance is given in parentheses. [c]Experimental parameters from ref 94. [d]Obtained from INDO/S−CI calculations on QM/MM optimized active-site models.

QM/MM optimized model, while scoring slightly poorer than the corresponding X-ray structure, provides a reasonable protein-structure description on the basis of stereochemical considerations. An analysis of individual contributions to the G factor of $Mn^{3+}SOD_{1VEW}$ revealed that the lower G factor of the QM/MM optimized model mainly stems from slight deviations (<0.059 Å) of aromatic residues from planarity and generally poorer dihedral angles. Nonetheless, the PROCHECK analysis clearly demonstrates that QM/MM geometry optimizations with the basis sets and partitioning scheme chosen are well suited for generating realistic three-dimensional models of Mn-bound SOD species. In strong support of this assumption, parallel QM/MM computations performed on monomer A of *T. thermophilus* Mn^{3+}SOD (PDB file 3MDS)[101] afforded similarly good agreement between optimized and crystallographically determined structures (i.e., G factors of −0.31 and 0.17 were determined for the QM/MM optimized model and subunit A of the X-ray crystal structure, respectively).

Given the success of our QM/MM approach in predicting the overall structure of Mn^{3+}SOD, it is warranted to compare the relevant bond lengths and bond angles of the $Mn^{3+}SOD_{1VEW}$ and $Mn^{3+}(Fe)SOD_{1ISB}$ active sites. The optimized Mn^{3+}−ligand (L) bond lengths of our $Mn^{3+}SOD_{1VEW}$ model are consistently shorter than their corresponding crystallographic values (Table 2),[7] reflecting the manganese redox heterogeneity in the crystals used for the X-ray structural analysis. This discrepancy between experimental and computed Mn^{3+}−L bond distances has been repeatedly observed in computational studies of Mn^{3+}SOD[11,45,83,85,90,102] and underscores the importance of computations for obtaining accurate Mn^{3+}−L bond distances for this species. In contrast, all L−Mn^{3+}−L′ angles of our $Mn^{3+}SOD_{1VEW}$ model are in excellent agreement with those determined experimentally (Table 2), implying that the bond angles are largely independent of the metal ion oxidation state. It is interesting to note that previous computational studies using truncated active-site models yielded much poorer agreement between the computed and crystallographic L−Mn^{3+}−L′ bond angles, with deviations approaching 20°.[85,90] In general, however, the active site of our QM/MM optimized $Mn^{3+}SOD_{1VEW}$ model, which incorporates steric effects of the protein monomer on the geometry of the active site, shows little structural deviations from DFT-optimized truncated models,[83,102] indicating that the Mn^{3+}SOD active site geometry is only weakly constrained by the protein matrix.

All Mn^{3+}−L bond distances in our $Mn^{3+}(Fe)SOD_{1ISB}$ model are very similar to the corresponding distances in the $Mn^{3+}SOD_{1VEW}$ model (Table 2), which is not surprising given the identical first coordination spheres of these two species. Nonetheless, as illustrated in Table 2, these models actually differ considerably in two regards, (i) the equatorial L−Mn^{3+}−L′ bond angles and (ii) the H-bonding distances between Gln146(69) and the coordinated solvent. While this last difference can be attributed to the different (Gln146(69))-N···O(sol) distances in the X-ray crystal structures of *E. coli* Mn^{3+}SOD and Fe^{3+}SOD (2.89 and 3.41 Å, respectively[6,7]) the other structural difference is surprising, as the equatorial bond angles in Mn- and FeSODs are comparable.[6,7] It is particularly intriguing that our $Mn^{3+}(Fe)SOD_{1ISB}$ model exhibits a rather small equatorial (His)N−Mn−N(His) bond angle of ∼110°, while in the X-ray crystal structure of Fe^{3+}(Mn)SOD this angle is unusually large (∼148°).[91] Overall, this comparison of the active-site structures of Mn^{3+}SOD, Mn^{3+}(Fe)SOD, and Fe^{3+}(Mn)SOD suggests that the (Fe)SOD protein matrix favors a more acute equatorial (His)N−metal−N(His) bond angle and a longer (Gln146(69))N···O(sol) distance than the (Mn)SOD protein matrix, factors that likely contribute to differences in the inner-sphere anion-binding affinities and E_m values between the WT and metal-substituted SODs.

(B). Computed Spectroscopic Properties of Mn^{3+}SOD and Mn^{3+}(Fe)SOD Models. The absorption spectra and ground-state ZFS parameters of the active sites of our $Mn^{3+}SOD_{1VEW}$ and $Mn^{3+}(Fe)SOD_{1ISB}$ models were computed using TD-DFT and INDO/S−CI methods, respectively. These computed spectroscopic properties permit further validation of our active-site models of Mn^{3+}SOD and Mn^{3+}(Fe)SOD on the basis of experimental data and allow for a quantitative comparison of the electronic structures of these sites.

The TD-DFT computed absorption spectra for $Mn^{3+}SOD_{1VEW}$ and $Mn^{3+}(Fe)SOD_{1ISB}$ (Figure 6, top and bottom)[103] agree remarkably well with their experimental counterparts (Figures 4 and 3, respectively), indicating that the active-site structures of these models are consistent with our spectroscopic data. Most importantly, the Mn^{3+} d → d

dx.doi.org/10.1021/ic302867y | Inorg. Chem. 2013, 52, 3356−3367

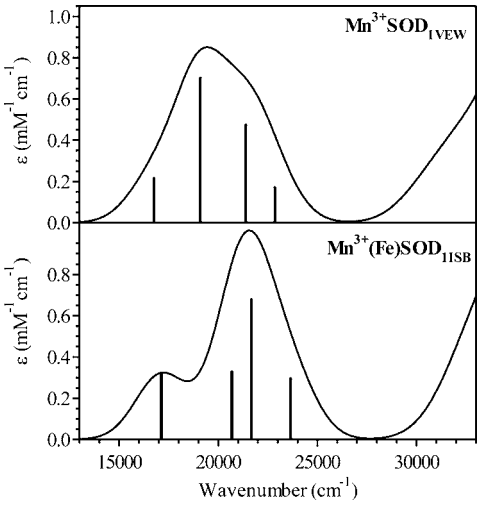

Figure 6. TD-DFT computed absorption spectra for the active-site models of $Mn^{3+}SOD_{1VEW}$ (top) and $Mn^{3+}(Fe)SOD_{1ISB}$ (bottom). The four spin-allowed Mn^{3+} d → d transitions are indicated by vertical sticks.

transition energies and intensities predicted for the $Mn^{3+}SOD_{1VEW}$ and $Mn^{3+}(Fe)SOD_{1ISB}$ models are quite similar (Figure 6, vertical sticks), as expected on the basis of the structural similarities between these two models (Table 2) and as required by our experimental data (Table 1). It is interesting to note, however, that the computed energy of the second Mn^{3+} d → d transition is significantly (~2000 cm^{-1}) higher for $Mn^{3+}(Fe)SOD$ than for $Mn^{3+}SOD$ (Figure 6). On the basis of spectroscopic studies of $Mn^{3+}SOD$, this transition was proposed to involve electronic excitation from the singly occupied Mn^{3+} $3d_{xy}$-based MO to the unoccupied Mn^{3+} $3d_{z^2}$-based MO;[89] thus, the energy of this transition relative to the other Mn^{3+} d → d transitions (all of which also terminate in the Mn^{3+} $3d_{z^2}$-based MO) is expected to be sensitive to perturbations in the equatorial plane. Considering that our $Mn^{3+}SOD_{1VEW}$ and $Mn^{3+}(Fe)SOD_{1ISB}$ models have considerably different equatorial L−Mn−L′ bond angles, the rather large difference in the energy of the Mn^{3+} $3d_{xy}$ → $3d_{z^2}$ transition (Figure 6) is therefore not surprising. While the Gaussian analyses of our absorption, CD, and, MCD spectra of $Mn^{3+}SOD$ and $Mn^{3+}(Fe)SOD$ reveal only minor differences in the energy of the second Mn^{3+} d → d transition (Table 1), the CD intensities for this transition are distinctly different (cf. Figures 3 and 4), in qualitative agreement with our computational prediction of a slight equatorial perturbation of the Mn^{3+} center in the metal-substituted protein. Thus, the small spectroscopic differences between $Mn^{3+}SOD$ and $Mn^{3+}(Fe)SOD$ (Figures 4 and 3) may be accounted for by the minor geometric differences between our $Mn^{3+}SOD_{1VEW}$ and $Mn^{3+}(Fe)SOD_{1ISB}$ models (Table 2).

The INDO/S−CI computations for $Mn^{3+}SOD_{1VEW}$ and $Mn^{3+}(Fe)SOD_{1ISB}$ predict that the active sites of these species give rise to virtually identical D values but a 2-fold larger rhombicity (E/D ratio) in the case of the metal-substituted enzyme. This result is in qualitative agreement with our finding that the VTVH MCD data fits for both proteins are relatively insensitive to the magnitude of E/D within the range of 0.1 to 0.33 (Supporting Information, Figures S1 and S2). From a comparison of the structures of our $Mn^{3+}(Fe)SOD_{1ISB}$ and $Mn^{3+}SOD_{1VEW}$ models (Table 2), the difference in the computed rhombicities may arise from differences in (i) second-sphere H-bonding interactions and/or (ii) equatorial L−Mn−L′ bond angles. The first possibility was assessed by performing INDO/S−CI computations on models of $Mn^{3+}(Fe)SOD_{1ISB}$ and $Mn^{3+}SOD_{1VEW}$ that included only the first coordination sphere. As in both cases the removal of Tyr34 and Gln146(69) had only minor effects on the INDO/S−CI computed ZFS parameters (Supporting Information, Tables S7 and S8), we conclude that second-sphere H-bonding interactions do not notably modulate the E/D values of $Mn^{3+}SOD$ and $Mn^{3+}(Fe)SOD$. In contrast, INDO/S−CI computations performed for a model of $Mn^{3+}(Fe)SOD_{1ISB}$ with the (His71)N−Mn−N(His160) bond angle increased to 125° yielded ZFS parameters quite similar to those computed for $Mn^{3+}SOD_{1VEW}$ (D = 1.17 and 1.18 cm^{-1}, and E/D = 0.115 and 0.099, respectively; cf. Table 2 and Supporting Information, Table S7). Collectively, these results suggest that in the case of Mn^{3+}-bound SODs, the ZFS parameters are most sensitive to the changes in the first coordination sphere.

Table 3. Relevant Structural and Zero-Field Splitting Parameters for $Mn^{2+}SOD$ and $Mn^{2+}(Fe)SOD$

	E. coli $Mn^{2+}SOD$ experimental[a]	$Mn^{2+}SOD_{1VEW}$ QM/MM	$Mn^{2+}(Fe)SOD_{1ISA}$ QM/MM
Mn−O(sol)	2.24	2.19	2.21
Mn−O(Asp167(156))	2.05	2.01	2.02
Mn−N(His26)	2.19	2.16	2.20
Mn−N(His171(160))	2.19	2.22	2.19
Mn−N(His81(73))	2.25	2.14	2.10
(His81(73))N−Mn−N(His171(160))	129°	123°	114°
(His81(73))N−Mn−N(Asp167(156))	110°	112°	118°
(His171(160))−Mn−N(Asp167(156))	120°	125°	128°
O(sol)−Mn−N(His26)	175°	175°	173°
O(sol)···O(Asp167(156))	2.75	2.51 (1.42)[b]	2.53 (1.47)[b]
(Gln146(69))N···O(sol)	2.89	2.98 (2.00)[b]	3.39 (2.60)[b]
(Gln146(69))N···O(Tyr34)	3.00	3.05 (2.28)[b]	3.04 (2.08)[b]
zero-field splitting parameters			
D (cm^{-1})	|0.3548|[c]	−0.058[d]	−0.068[d] (|0.3506|[c])
E/D	0.0860[c]	0.084[d]	0.048[d] (0.0405[c])

[a]Derived from the X-ray crystal structure of *E. coli* MnSOD (PDB file 1VEW).[7] [b]The corresponding H···O hydrogen-bond distance is given in parentheses. [c]Experimental parameters from ref 26. [d]Obtained from INDO/S−CI calculations on QM/MM optimized active-site models.

dx.doi.org/10.1021/ic302867y | *Inorg. Chem.* 2013, 52, 3356−3367

(C). Geometric Structures of Mn^{2+}SOD and Mn^{2+}(Fe)SOD Models. The QM/MM optimized active-site structures of the Mn^{2+}SOD and Mn^{2+}(Fe)SOD monomers (referred to as $Mn^{2+}SOD_{1VEW}$ and $Mn^{2+}(Fe)SOD_{1ISA}$, respectively) are quite distinct from those of their oxidized counterparts, particularly with respect to the metal−ligand bond lengths, which increase considerably upon metal-ion reduction (cf. Tables 2 and 3). While similar changes in metal−ligand bond lengths accompanying $Mn^{3+} \rightarrow Mn^{2+}$ reduction have been observed in previous computational studies,[11,83,85,90,102] our QM/MM computations reveal, for the first time, that the major structural differences between Mn^{2+}SOD and Mn^{2+}(Fe)SOD and between Mn^{3+}SOD and Mn^{3+}(Fe)SOD are similar in nature, primarily involving a smaller (His)N−Mn−N(His) bond angle and a longer (Gln146(69))N···O(sol) distance in the metal-substituted proteins (cf. Tables 3 and 2).[104] Therefore, these structural differences appear to reflect intrinsic differences between the (Fe)SOD and (Mn)SOD protein matrixes that are independent of the metal ion oxidation state.

(D). Computed Spectroscopic Properties of Mn^{2+}SOD and Mn^{2+}(Fe)SOD Models. The ZFS parameters obtained from HF-EPR studies of *E. coli* Mn^{2+}SOD and Mn^{2+}(Fe)SOD (Table 3)[26] provide a suitable basis for further validation of the active sites of our $Mn^{2+}SOD_{1VEW}$ and $Mn^{2+}(Fe)SOD_{1ISA}$ models using INDO/S−CI computations. In both cases, the INDO/S−CI computations reproduce the experimental *E/D* values remarkably well, though the *D* values are underestimated considerably (Table 3, bottom). Despite this deficiency, the computed ZFS parameters parallel the experimental trends quite nicely; that is, the computed *E/D* value for $Mn^{2+}(Fe)SOD_{1ISA}$ is roughly half of that computed for $Mn^{2+}SOD_{1VEW}$, while the computed *D* values for these models are virtually identical (Table 3, bottom). As the structural origin of the different rhombicities of Mn^{2+}SOD and Mn^{2+}(Fe)SOD is currently unclear, our computational models provide an excellent opportunity for exploring the dependence of the *E/D* ratio on geometric structure. Based upon the fact that the $Mn^{2+}SOD_{1VEW}$ and $Mn^{2+}(Fe)SOD_{1ISA}$ models exhibit distinct equatorial bond angles and second-sphere H-bonding distances, the dependence of *E/D* on these two structural parameters was evaluated. Interestingly, INDO/S−CI computations on a model of $Mn^{2+}(Fe)SOD_{1ISA}$ with the (His73)N−Mn−N(His160) bond angle increased to 124° afforded an *E/D* value of 0.048, identical to that predicted for the optimized model wherein which this angle is only 114° (cf. Tables 3 and Supporting Information, Table S9). In contrast, INDO/S−CI computations performed on active-site models of $Mn^{2+}SOD_{1VEW}$ and $Mn^{2+}(Fe)SOD_{1ISA}$ that included only the first coordination sphere predicted a greatly reduced *E/D* value of 0.061 for $Mn^{2+}SOD_{1VEW}$, but an unchanged *E/D* value of 0.048 for $Mn^{2+}(Fe)SOD_{1ISA}$ (cf. Table 3 and Supporting Information, Table S8). Collectively, these results suggest that for Mn^{2+}-bound SODs, the ZFS parameters are more sensitive to changes in the second rather than the first coordination sphere, exactly opposite to the case of Mn^{3+}-bound SODs.

To better understand how differences in second-sphere/first-sphere interactions between $Mn^{2+}SOD_{1VEW}$ and $Mn^{2+}(Fe)SOD_{1ISA}$ could lead to different ground-state properties, natural bond orbital (NBO) computations were carried out. These computations describe H-bonding interactions in terms of a donor/acceptor model that treats a H-bond as charge transfer between a lone pair (donor) NBO (σ_d) and an antibonding (acceptor) NBO (σ_a*).[62,63] Within this formalism the strength of the donor/acceptor interaction, and thus the strength of the H-bond, can be quantified by using second-order perturbation theory (eq 3).[62,63] Additionally, qualitative insight into the strength of a H-bond can be obtained by visual inspection of the overlap of the pre-NBOs that correspond to the donor and acceptor NBOs, as large overlap between these pre-NBOs is associated with a large second-order energy correction (eq 3) and thus signifies a strong H-bonding interaction.[62,63] Plots of the O(sol) lone pair pre-NBOs (corresponding to σ_d) and the (Gln146(69))N−H antibonding pre-NBOs (σ_a*) for $Mn^{2+}SOD_{1VEW}$ and $Mn^{2+}(Fe)SOD_{1ISA}$ reveal significantly larger overlap in the former case (Figure 7). The larger overlap for

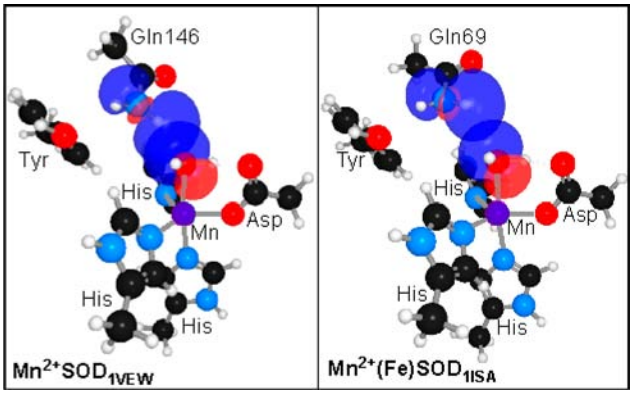

Figure 7. Plots of the lone pair pre-NBOs of the coordinated solvent (σ_d) and the antibonding pre-NBOs of (Gln146(69))N−H (σ_a*) for $Mn^{2+}SOD_{1VEW}$ (left) and $Mn^{2+}(Fe)SOD_{1ISA}$ (right). Note that the vastly different overlaps of the σ_d/σ_a* orbitals in the two species reflect a much stronger H-bond interaction in the native enzyme.

$Mn^{2+}SOD_{1VEW}$ is a consequence of the significantly shorter (Gln146)NH···O(sol) H-bond distance in this species (2.00 Å) compared to the corresponding (Gln69)NH···O(sol) distance in $Mn^{2+}(Fe)SOD_{1ISA}$ (2.60 Å). Quantitatively, the stronger H-bond for $Mn^{2+}SOD_{1VEW}$ is represented by the large second-order energy correction of ∼10 kcal/mol, compared with the virtually negligible correction of ∼1 kcal/mol for $Mn^{2+}(Fe)$-SOD_{1ISA}. Taken together, these NBO computations suggest that it is the strong H-bond interactions between Gln146 and coordinated solvent that markedly perturb the ZFS parameters of $Mn^{2+}SOD_{1VEW}$, providing an appealing rationale for the differences in the experimentally determined ZFS parameters of Mn^{2+}SOD and Mn^{2+}(Fe)SOD.[26] These results also nicely complement those obtained from ^{15}N NMR studies of Fe^{2+}SOD and Fe^{2+}(Mn)SOD, which revealed stronger coupling between the Gln146 amide group and the ferrous center in the latter protein.[105]

3.3. Computation of Reduction Potentials for MnSOD and Mn(Fe)SOD. MnSOD and Mn(Fe)SOD exhibit reduction midpoint potentials that differ by at least 700 mV.[22] Using our DFT single-point energies with point charge corrections, in conjunction with eqs 4−6, we computed E_m values of +330 mV for the $Mn^{3+}SOD^{OH} \rightarrow Mn^{2+}SOD^{H2O}$ conversion and +1.72 V for the $Mn^{3+}(Fe)SOD^{OH} \rightarrow Mn^{2+}(Fe)SOD^{H2O}$ conversion (both at pH 7.8). These computed potentials are in excellent agreement with the experimental values (E_m = 290 mV and >960 mV for MnSOD and Mn(Fe)SOD, respectively[22]) both in terms of absolute potentials as well as the large increase in redox potential from MnSOD to Mn(Fe)SOD (calculated difference of ∼1.4 V vs >700 mV observed experimentally).

dx.doi.org/10.1021/ic302867y | *Inorg. Chem.* 2013, 52, 3356−3367

4. DISCUSSION

Given the structural homology of Fe- and MnSODs, the lack of catalytic activity displayed by the metal-substituted SODs (i.e., Mn(Fe)SOD and Fe(Mn)SOD) has long puzzled chemists and biologists.[16] While it has been shown quite conclusively that the lack of activity of *E. coli* Mn(Fe)SOD derives principally from its high E_m,[22] the structural basis for the altered E_m of Mn(Fe)SOD has remained ambiguous, as to date no X-ray crystal structure of this species exists. In this study, we have used QM/MM computations to generate models of *E. coli* Mn^{3+}(Fe)SOD and Mn^{2+}(Fe)SOD starting from the FeSOD X-ray crystal structures, and validated the active site descriptions of these models on the basis of spectroscopic data. The results of our combined spectroscopic/computational approach offer insight into the origin of the lack of activity of Mn(Fe)SOD and provide clues as to how the (Fe)- and (Mn)SOD protein matrixes modulate active site/substrate analogue interactions, as discussed below.

4.1. Efficacy of QM/MM Geometry Optimizations. The QM/MM geometry optimizations using the functional, basis sets, and partitioning scheme described in the Experimental Section yielded protein structures that are in excellent agreement with experimental data (Tables 2 and 3). The equatorial L−Mn−L′ bond angles in the QM/MM optimized models of Mn^{3+}SOD and Mn^{2+}SOD are virtually identical to those obtained using X-ray crystallography, which represents a major improvement over the structures obtained using truncated active-site models.[45,85,90] As these angles change dramatically upon the coordination of small anions to the metal ion (e.g., Mn^{3+}SOD and its corresponding azide adduct exhibit equatorial (His)N−Mn−N(His) angles of 129° and 148°, respectively[6,7]), the ability of our QM/MM computations to predict accurate equatorial bond angles suggests that this approach may also have distinct advantages over the use of truncated active-site models for computational studies of active-site/anion interactions.

4.2. Origin of Elevated E_m of Mn(Fe)SOD. The close correspondence between the spectroscopic and computational data obtained for Mn^{3+}SOD and Mn^{3+}(Fe)SOD demonstrates that these species possess virtually identical active sites consisting of a Mn^{3+} ion in a trigonal bipyramidal ligand environment. Yet, a previous HF-EPR study of the reduced proteins revealed that Mn^{2+}(Fe)SOD gives rise to a more axial EPR spectrum than that of Mn^{2+}SOD,[26] perhaps reflecting an altered active-site geometry in the metal-substituted protein. However, INDO/S−CI computation performed on our QM/MM optimized models of $Mn^{2+}SOD_{1VEW}$ and Mn^{2+}(Fe)-SOD_{1ISA}, which exhibit very similar active-site structures (Table 3), yielded *E/D* values of 0.084 and 0.048, respectively, in remarkable agreement with the corresponding experimental values (0.0860 and 0.0405).[26] Our NBO computations support the notion that the different ZFS parameters of Mn^{2+}(Fe)SOD and Mn^{2+}SOD are not linked to differences in the first coordination sphere but instead reflect distinct Gln(146(69))-NH···O(sol) H-bonding interactions (Figure 7). Collectively, the spectroscopic and computational data provide compelling evidence that the lack of catalytic activity of Mn(Fe)SOD is not due to gross active site distortions in either the oxidized or the reduced state.

Despite its WT-like active-site structure, Mn(Fe)SOD possesses an E_m (>970 mV) that is dramatically elevated over that of MnSOD (~290 mV),[22] demonstrating that the (Fe)SOD and (Mn)SOD protein matrixes exert tremendous control over the E_m of the bound metal ion. While a number of mechanisms exist by which a protein matrix can modulate the E_m of a metal ion, probably the most obvious involves a direct tuning of the energy of the redox-active MO. In the case of MnSOD and Mn(Fe)SOD, this tuning could be achieved through modulation of the energy of the unoccupied Mn^{3+} $3d_{z^2}$-based MO that accepts an electron upon $Mn^{3+} \rightarrow Mn^{2+}$ reduction. However, the virtually identical absorption, CD, and MCD spectra of Mn^{3+}(Fe)SOD and Mn^{3+}SOD (cf. Figures 3 and 4) show that both the splittings of the Mn^{3+} d-based MOs and the energies of these orbitals relative to those of the ligand-based MOs are nearly identical in these two species. Thus, these spectra do not support a mechanism of redox tuning wherein which the (Mn)SOD and (Fe)SOD protein matrixes differently tune the energies of the redox-active MOs.

An alternative mechanism by which these protein matrixes could differently tune the metal ion E_m involves the creation of an active-site environment that differentially stabilizes the preferred geometry of one oxidation state versus that of the other. Our QM/MM computations suggest that this could be achieved by (i) second-sphere H-bonding interactions and/or (ii) modulation of the equatorial L−Mn−L′ bond angles, as these are the only major structural differences between our experimentally validated Mn(Fe)SOD and MnSOD models (Tables 2 and 3). As the altered equatorial L−Mn−L′ bond angles will similarly affect the energies of all occupied MOs in the oxidized and reduced states and are thus unlikely to play a role in the E_m tuning mechanism, we propose that the considerably different E_m values of Mn(Fe)SOD and MnSOD stem from the vastly different Gln(146(69))NH···O(sol) interactions in these species. Specifically, the larger separation between the second-sphere Gln residue and the coordinated solvent in Mn(Fe)SOD relative to MnSOD causes a weakening of the corresponding H-bond interaction in the oxidized state and alleviates steric crowding in the reduced state.

This proposal is supported by an extensive body of literature that clearly demonstrates a key role for Gln146(69) in E_m tuning.[21,24,106−110] Hence, the (Mn)SOD and (Fe)SOD protein matrixes most elegantly exploit the fact that the protonation state of the coordinated solvent differs in the oxidized and reduced states of the enzymes (eq 1), which allows Gln146(69) to influence the p*K* of the coordinated solvent and, thus, to modulate the relative energy of a given metal ion oxidation state through H-bonding and steric interactions.[22,22] In further support of this proposal, DFT/electrostatics computations by Noodleman and co-workers suggested that the p*K* values of the coordinated H_2O molecules of WT and Q146N Mn^{2+}SODs (where the Gln146 residue was replaced with an Asn) differ by nearly 7 pH units.[11] Accordingly, the calculated E_m for Q146N MnSOD was nearly 200 mV higher than the computed value for the WT enzyme,[11] consistent with experimental data that demonstrated a substantially increased E_m value for this variant SOD.[108]

The different positioning of the second-sphere Gln146(69) residues in the (Fe)SOD and (Mn)SOD protein matrixes has also been shown to be largely responsible for the drastically depressed E_m value of Fe(Mn)SOD. Specifically, our studies using QM/MM whole protein optimizations and DFT calculated redox potentials found that there is little difference (0.051 eV) between FeSOD and Fe(Mn)SOD when comparing the computed energies for the electron transfer step, but instead the differences in the overall E_m's mostly

dx.doi.org/10.1021/ic302867y | *Inorg. Chem.* 2013, 52, 3356−3367

comes from their vastly different energies (0.97 eV versus 0.51 eV for FeSOD and Fe(Mn)SOD, respectively) for the proton transfer step.[24] Additionally, when using truncated models comprising only the first coordination sphere our computations predicted E_m's that differed by only 80 mV.[24] Combined, these computations emphasize the important role that the positioning of Gln146(69) plays in modulating the proton affinity of the coordinated solvent molecule in the reduced (Fe^{2+}) form of these enzymes so as to properly tune their overall E_m's.

■ ASSOCIATED CONTENT

Ⓢ Supporting Information

Zero-field splitting parameters, transition polarizations, and χ^2 values obtained from fits of the VTVH MCD data of Mn^{3+}(Fe)SOD and Mn^{3+}SOD (Figures S1 and S2, Tables S5 and S6), ZFS parameters computed for the Mn(Fe)SOD and MnSOD active-site models (Tables S7–S9), active spaces used for the INDO/S–CI computations, and Cartesian coordinates for the active sites of all QM/MM optimized protein models (Tables S1–S4). This material is available free of charge via the Internet at http://pubs.acs.org.

■ AUTHOR INFORMATION

Corresponding Author

*Phone: (608) 265-9056. Fax: (608) 262-6143. E-mail: Brunold@chem.wisc.edu.

Notes

The authors declare no competing financial interest.

■ ACKNOWLEDGMENTS

T.C.B. thanks the NIH (GM 64631) for financial support and acknowledges Dr. Frank Neese (MPI Mülheim) for providing a free copy of ORCA and for useful discussions. A.-F.M. acknowledges financial support by the NSF (MCB0129599) and NIH (GM 85302). This research was supported in part by National Science Foundation Grant CHE-0840494.

■ REFERENCES

(1) Miller, A.-F.; Sorkin, D. L. *Comments Mol. Cell. Biophys.* **1997**, *9*, 1–48.

(2) Miller, A.-F. Superoxide processing. In *Comprehensive Coordination Chemistry II*,; McCleverty, J. A., Meyer, T. J., Eds.; Elsevier Ltd.: Oxford, U.K., 2004; Vol. *8*, pp 479–506.

(3) Miller, A.-F. *Curr. Opin. Chem. Biol.* **2004**, *8*, 162–168.

(4) Packer, L. *Methods in Enzymology: Superoxide Dismutase*; Academic Press: San Diego, CA, 2002; Vol. *349*, p 400.

(5) The numbering scheme used here relates to *E. coli* MnSOD and, in parentheses, FeSOD if different. For clarity, the *E. coli* numbering scheme will be used throughout.

(6) Lah, M. S.; Dixon, M. M.; Pattridge, K. A.; Stallings, W. C.; Fee, J. A.; Ludwig, M. L. *Biochemistry* **1995**, *34*, 1646–1660.

(7) Edwards, R. A.; Baker, H. M.; Whittaker, M. M.; Whittaker, J. W.; Jameson, G. B.; Baker, E. N. *J. Biol. Inorg. Chem.* **1998**, *3*, 161–171.

(8) Stallings, W. C.; Metzger, A. L.; Pattridge, K. A.; Fee, J. A.; Ludwig, M. L. *Free Radical Res. Commun.* **1991**, *12–13*, 259–268.

(9) Tierney, D. L.; Fee, J. A.; Ludwig, M. L.; Penner-Hahn, J. E. *Biochemistry* **1995**, *34*, 1661–1668.

(10) Miller, A.-F.; Padmakumar, F.; Sorkin, D.; Karapetian, A.; Vance, C. K. *J. Inorg. Biochem.* **2003**, *93*, 71–83.

(11) Han, W.-G.; Lovell, T.; Noodleman, L. *Inorg. Chem.* **2002**, *41*, 205–218.

(12) Lavelle, F.; McAdam, M. E.; Fielden, E. M.; Roberts, P. B.; Puget, K.; Michelson, A. M. *Biochem. J.* **1977**, *161*, 3–11.

(13) Pick, M.; Rabani, J.; Yost, F.; Fridovich, I. *J. Am. Chem. Soc.* **1974**, *96*, 7329–7333.

(14) Bull, C.; Fee, J. A. *J. Am. Chem. Soc.* **1985**, *107*, 3295–3304.

(15) Hsu, J. L.; Hsieh, Y. S.; Tu, C. K.; O'Connor, D.; Nick, H. S.; Silverman, D. N. *J. Biol. Chem.* **1996**, *271*, 17687–17691.

(16) Ose, D. E.; Fridovich, I. *J. Biol. Chem.* **1976**, *251*, 1217–1218.

(17) Yamakura, F. *J. Biochem.* **1978**, *83*, 849–857.

(18) Whittaker, M. M.; Whittaker, J. W. *Biochemistry* **1997**, *36*, 8923–8931.

(19) Yamakura, F.; Kobayashi, K.; Ue, H.; Konno, M. *Eur. J. Biochem.* **1995**, *227*, 700.

(20) All E_m values are versus the normal hydrogen electrode (NHE).

(21) Vance, C. K.; Miller, A.-F. *J. Am. Chem. Soc.* **1998**, *120*, 461–467.

(22) Vance, C. K.; Miller, A. F. *Biochemistry* **2001**, *40*, 13079–13087.

(23) Jackson, T. A.; Xie, J.; Yikilmaz, E.; Miller, A.-F.; Brunold, T. C. *J. Am. Chem. Soc.* **2002**, *124*, 10833–10845.

(24) Grove, L. E.; Xie, J.; Yikilmaz, E.; Miller, A.-F.; Brunold, T. C. *Inorg. Chem.* **2008**, *47*, 3978–3992.

(25) Vance, C. K.; Miller, A.-F. *Biochemistry* **1998**, *37*, 5518–5527.

(26) Un, S.; Tabares, L. C.; Cortez, N.; Hiraoka, B. Y.; Yamakura, F. *J. Am. Chem. Soc.* **2004**, *126*, 2720–2726.

(27) Sorkin, D. L.; Miller, A.-F. *Biochemistry* **1997**, *36*, 4916–4924.

(28) Slykhouse, T. O.; Fee, J. A. *J. Biol. Chem.* **1976**, *251*, 5472–5477.

(29) Neese, F.; Solomon, E. I. *Inorg. Chem.* **1999**, *38*, 1847–1865.

(30) Jackson, T. A.; Karapetian, A.; Miller, A.-F.; Brunold, T. C. *Biochemistry* **2005**, *44*, 1504–1520.

(31) Krzystek, J.; Fiedler, A. T.; Sokol, J. J.; Ozarowski, A.; Zvyagin, S. A.; Brunold, T. C.; Long, J. R.; Brunel, L.-C.; Telser, J. *Inorg. Chem.* **2004**, *43*, 5645–5658.

(32) Krzystek, J.; Zvyagin, S. A.; Ozarowski, A.; Fiedler, A. T.; Brunold, T. C.; Telser, J. *J. Am. Chem. Soc.* **2004**, *126*, 2148–2155.

(33) te Velde, G.; Bickelhaupt, F. M.; van Gisbergen, S. J. A.; Guerra, C. F.; Baerends, E. J.; Snijders, J. G.; Ziegler, T. *J. Comput. Chem.* **2001**, *22*, 931–967.

(34) Guerra, C. F.; Snijders, J. G.; te Velde, G.; Baerends, E. J. *Theor. Chem. Acc.* **1998**, *99*, 391–403.

(35) *ADF2003.01*; SCM, Theoretical Chemistry, Vrije Universiteit: Amsterdam, The Netherlands; http://www.scm.com.

(36) Vosko, S. H.; Wilk, L.; Nusair, M. *Can. J. Phys.* **1980**, *58*, 1200–1211.

(37) Becke, A. D. *J. Chem. Phys.* **1986**, *84*, 4524–4529.

(38) Perdew, J. P. *Phys. Rev. B* **1986**, *33*, 8822–8824.

(39) Cornell, W. D.; Cieplak, P.; Bayly, C. I.; Gould, I. R.; Merz, K. M.; Ferguson, D. M.; Spellmeyer, D. C.; Fox, T.; Caldwell, J. W.; Kollman, P. A. *J. Am. Chem. Soc.* **1995**, *117*, 5179–5197.

(40) We used a molecular weight of 54.94 g/mol and specified no potential as the van der Waals potential type for manganese in the AMBER95 force field file. As manganese is in the QM region, these parameters do not affect the computations.

(41) Maseras, F.; Morokuma, K. *J. Comput. Chem.* **1995**, *16*, 1170–1179.

(42) Woo, T. K.; Cavallo, L.; Ziegler, T. *Theor. Chem. Acc.* **1998**, *100*, 307–313.

(43) Swart, M.; van Duijnen, P. T.; Snijders, J. G. *J. Comput. Chem.* **2000**, *22*, 79–88.

(44) Neese, F. *ORCA – an ab initio, Density Functional and Semiempirical Program Package*, Version 2.2; Max Planck Institut für Strahlenchemie: Mülheim, Germany, 2002.

(45) Jackson, T. A.; Karapetian, A.; Miller, A.-F.; Brunold, T. C. *J. Am. Chem. Soc.* **2004**, *126*, 12477–12491.

(46) Ridley, J.; Zerner, M. C. *Theor. Chim. Acta* **1973**, *32*, 111–134.

(47) Zerner, M. C.; Loew, G. H.; Kirchner, R. F.; Mueller-Westerhof, U. T. *J. Am. Chem. Soc.* **1980**, *102*, 589–599.

(48) Bacon, A. D.; Zerner, M. C. *Theor. Chim. Acta* **1979**, *53*, 21–54.

(49) Bauernschmitt, R.; Ahlrichs, R. *Chem. Phys. Lett.* **1996**, *256*, 454–464.

(50) Casida, E. M.; Jamorski, C.; Casida, K. C.; Salahub, D. R. *J. Chem. Phys.* **1998**, *108*, 4439–4449.

(51) Stratman, R. E.; Scuseria, G. E.; Frisch, M. J. *J. Chem. Phys.* **1998**, *109*, 8218–8224.

(52) Becke, A. D. *J. Chem. Phys.* **1993**, *98*, 1372−1377.
(53) Becke, A. D. *J. Chem. Phys.* **1993**, *98*, 5648−5652.
(54) Lee, C.; Yang, W.; Parr, R. G. *Phys. Rev. B* **1988**, *37*, 785−789.
(55) Schäfer, A.; Horn, H.; Ahlrichs, R. *J. Chem. Phys.* **1992**, *97*, 2571−2577.
(56) Ahlrichs, R., unpublished results.
(57) The Ahlrichs auxiliary basis sets were obtained from the TurboMole basis set library found under ftp.chemie.uni-karlsruhe.de/pub/cbasen. Weigend, F.; Häser, M. *Theor. Chem. Acc.* **1997**, *97*, 331−340.
(58) Schäfer, G.; Huber, C.; Ahlrichs, R. *J. Chem. Phys.* **1994**, *100*, 5829−5835.
(59) Hirata, S.; Head-Gordon, M. *Chem. Phys. Lett.* **1999**, *302*, 375−382.
(60) Hirata, S.; Head-Gordon, M. *Chem. Phys. Lett.* **1999**, *314*, 291−299.
(61) Neese, F.; Olbrich, G. *Chem. Phys. Lett.* **2002**, *362*, 170−178.
(62) Weinhold, F.; Landis, C. R., *Chem. Ed.: Res. Practice Eur.* **2001**, *2*, 91-104.
(63) Reed, A. E.; Curtiss, L. A.; Weinhold, F. *Chem. Rev.* **1988**, *88*, 899−926.
(64) Glendening, E. D.; Badenhoop, J, K.; Reed, A. E.; Carpenter, J. E.; Bohmann, J. A.; Morales, C. M.; Weinhold, F. *NBO*, 5.0; Theoretical Chemistry Institute, University of Wisconsin: Madison, WI, 2001.
(65) Frisch, M. J.; Trucks, G. W.; Schlegel, H. B.; Scuseria, G. E.; Robb, M. A.; Cheeseman, J. R.; Montgomery, J., J. A.; Vreven, T.; Kudin, K. N.; Burant, J. C.; Millam, J. M.; Iyengar, S. S.; Tomasi, J.; Barone, V.; Mennucci, B.; Cossi, M.; Scalmani, G.; Rega, N.; Petersson, G. A.; Nakatsuji, H.; Hada, M.; Ehara, M.; Toyota, K.; Fukuda, R.; Hasegawa, J.; Ishida, M.; Nakajima, T.; Honda, Y.; Kitao, O.; Nakai, H.; Klene, M.; Li, X.; Knox, J. E.; Hratchian, H. P.; Cross, J. B.; Adamo, C.; Jaramillo, J.; Gomperts, R.; Stratmann, R. E.; Yazyev, O.; Austin, A. J.; Cammi, R.; Pomelli, C.; Ochterski, J. W.; Ayala, P. Y.; Morokuma, K.; Voth, G. A.; Salvador, P.; Dannenberg, J. J.; Zakrzewski, V. G.; Dapprich, S.; Daniels, A. D.; Strain, M. C.; Farkas, O.; Malick, D. K.; Rabuck, A. D.; Raghavachari, K.; Foresman, J. B.; Ortiz, J. V.; Cui, Q.; Baboul, A. G.; Clifford, S.; Cioslowski, J.; Stefanov, B. B.; Liu, G.; Liashenko, A.; Piskorz, P.; Komaromi, I.; Martin, R. L.; Fox, D. J.; Keith, T.; Al-Laham, M. A.; Peng, C. Y.; Nanayakkara, A.; Challacombe, M.; Gill, P. M. W.; Johnson, B.; Chen, W.; Wong, M. W.; Gonzalez, C.; Pople, J. A. *Gaussian 98*; Gaussian Inc.: Pittsburgh, PA, 1998.
(66) Ditchfield, R.; Hehre, W. J.; Pople, J. A. *J. Chem. Phys.* **1971**, *54*, 724−728.
(67) Hehre, W. J.; Ditchfield, R.; Pople, J. A. *J. Chem. Phys.* **1972**, *56*, 2257−2261.
(68) Hariharan, P. C.; Pople, J. A. *Mol. Phys.* **1974**, *27*, 209−214.
(69) Gordon, M. S. *Chem. Phys. Lett.* **1980**, *76*, 163−168.
(70) Hariharan, P. C.; Pople, J. A. *Theor. Chim. Acta* **1973**, *28*, 213−222.
(71) Wachters, A. J. *J. Chem. Phys.* **1970**, *52*, 1033.
(72) Hay, P. J. *J. Chem. Phys.* **1977**, *66*, 4377−4384.
(73) Raghavachari, K.; Trucks, G. W. *J. Chem. Phys.* **1989**, *91*, 1062−1065.
(74) Binkley, J. S.; Pople, J. A.; Hehre, W. J. *J. Am. Chem. Soc.* **1980**, *102*, 939−947.
(75) Gordon, M. S.; Binkley, J. S.; Pople, J. A.; Pietro, W. J.; Hehre, W. J. *J. Am. Chem. Soc.* **1982**, *104*, 2797−2803.
(76) Pietro, W. J.; Francl, M. M.; Hehre, W. J.; Defrees, D. J.; Pople, J. A.; Binkley, J. S. *J. Am. Chem. Soc.* **1982**, *104*, 5039−5048.
(77) Dobbs, K. D.; Hehre, W. J. *J. Comput. Chem.* **1986**, *7*, 359−378.
(78) Dobbs, K. D.; Hehre, W. J. *J. Comput. Chem.* **1987**, *8*, 880−893.
(79) Dobbs, K. D.; Hehre, W. J. *J. Comput. Chem.* **1987**, *8*, 861−879.
(80) Pre-NBOs are the nonorthogonal precursors of NBOs. Pre-NBOs are orthogonal with other pre-NBOs on the same atom but have nonvanishing overlap with pre-NBOs on other atoms.
(81) Wendt, M.; Weinhold, F. *NBO View*; Theoretical Chemistry Institute, University of Wisconsin: Madison, WI, 2001.
(82) Li, J.; Fisher, C. L.; Chen, J. L.; Bashford, D.; Noodleman, L. *Inorg. Chem.* **1996**, *35*, 4694−4702.
(83) Li, J.; Fisher, C. L.; Konecny, R.; Lovell, T.; Bashford, D.; Noodleman, L. *Inorg. Chem.* **1999**, *38*, 929−939.
(84) Fisher, C. L.; Li, J.; Chen, J. L.; Bashford, D.; Noodleman, L. *Chem. Abstr.* **1995**, *209*, 153.
(85) Fisher, C. L.; Chen, J. L.; Li, J.; Bashford, D.; Noodleman, L. *J. Phys. Chem.* **1996**, *100*, 13498−13505.
(86) SCM/Theoretical Chemistry-Vrije Universiteit; *ADF QM/MM Manual*; Scientific Computing & Modelling NV: Amsterdam; The Netherlands, 2012.
(87) Neese, F. *ORCA - an ab initio, Density Functional and Semiempirical Program Package*, Version 2.9.1; Max Planck Institut für Strahlenchemie: Mülheim, Germany, 2012.
(88) The increase in absorption intensity above 25 000 cm^{-1} is due primarily to light scattering from the frozen sample at 4.5 K.
(89) Whittaker, J. W.; Whittaker, M. M. *J. Am. Chem. Soc.* **1991**, *113*, 5528−5540.
(90) Whittaker, M. M.; Ekberg, C. A.; Edwards, R. A.; Baker, E. N.; Jameson, G. B.; Whittaker, J. W. *J. Phys. Chem. B* **1998**, *102*, 4668−4677.
(91) Edwards, R. A.; Whittaker, M. M.; Whittaker, J. W.; Jameson, G. B.; Baker, E. N. *J. Am. Chem. Soc.* **1998**, *120*, 9684−9685.
(92) Oganesyan, V. S.; George, S. J.; Cheesman, M. R.; Thomson, A. J. *J. Chem. Phys.* **1999**, *110*, 762−777.
(93) INDO/S-CI computations predict the *z*- and *y*-axis of the **D**-tensors of Mn^{3+}SOD and Mn^{3+}(Fe)SOD to be oriented roughly along the Mn−O(sol) and Mn−N(His81(73)) bond vectors, respectively.
(94) Campbell, K. A.; Yikilmaz, E.; Grant, C. V.; Gregor, W.; Miller, A.-F.; Britt, R. D. *J. Am. Chem. Soc.* **1999**, *121*, 4714−4715.
(95) Mantel, C.; Philouze, C.; Collomb, M.-N.; Duboc, C. *Eur. J. Inorg. Chem.* **2004**, 3880−3886.
(96) Mantel, C.; Hassan, A. K.; Pécaut, J.; Deronzier, A.; Collomb, M.-N.; Duboc-Toia, C. *J. Am. Chem. Soc.* **2003**, *125*, 12337−12344.
(97) Un, S.; Dorlet, P.; Voyard, G.; Tabares, L. C.; Cortez, N. *J. Am. Chem. Soc.* **2001**, *123*, 10123−10124.
(98) Jackson, T. A.; Xie, J.; Yikilmaz, E.; Miller, A.-F.; Brunold, T. C. *J. Am. Chem. Soc.* **2002**, *124*, 10833−10845.
(99) Morris, A. L.; MacArthur, M. W.; Hutchinson, E. G.; Thornton, J. M. *Proteins* **1992**, *12*, 345−364.
(100) Laskowski, R. A.; MacArthur, M. W.; Moss, D. S.; Thornton, J. M. *J. Appl. Crystallogr.* **1993**, *26*, 283−291.
(101) Ludwig, M. L.; Metzger, A. L.; Pattridge, K. A.; Stallings, W. C. *J. Mol. Biol.* **1991**, *219*, 335−358.
(102) Whittaker, J. *Int. J. Quantum Chem.* **2002**, *90*, 1529−15635.
(103) For these simulations it was assumed that each electronic transition can be described by a Gaussian band with a full width at half-maximum ($\nu_{1/2}$) of 3 000 cm^{-1}, in which case the oscillator strength (f_{calc}) of the electronic transition is related to its molar extinction coefficient ε_{max} (M^{-1} cm^{-1}) by $f_{calc} = 4.61 \times 10^{-9}\ \varepsilon_{max}\ \nu_{1/2}$.
(104) Note, however, that the (Gln146(69))N···O(Tyr34) distances for the Mn^{2+}-bound SODs are virtually identical (Table 3).
(105) Schwartz, A. L.; Yikilmaz, E.; Vance, C. K.; Vathyam, S.; Miller, A.-F. *J. Inorg. Biochem.* **2000**, *80*, 247−256.
(106) Hiraoka, B. Y.; Yamakura, F.; Sugio, S.; Nakayama, K. *Biochem. J.* **2000**, *345*, 345−350.
(107) Lévêque, V. J.-P.; Vance, C. K.; Nick, H. S.; Silverman, D. N. *Biochemistry* **2001**, *40*, 10586−10591.
(108) Hsieh, Y. S.; Guan, Y.; Tu, C. K.; Bratt, P. J.; Angerhofer, A.; Lepock, J. R.; Hickey, M. J.; Tainer, J. A.; Nick, H. S.; Silverman, D. N. *Biochemistry* **1998**, *37*, 4731−4739.
(109) Yamakura, F.; Sugio, S.; Hiraoka, B. Y.; Ohmori, D.; Yokota, T. *Biochemistry* **2003**, *42*, 10790−10799.
(110) Yikilmaz, E.; Rodgers, D. W.; Miller, A.-F. *Biochemistry* **2006**, *45*, 1151−1161.